Aberystwyth University

Melt-Quenched Glasses of Metal–Organic Frameworks

Bennett, Thomas D.; Yue, Yuanzheng; Li, Peng; Qiao, Ang; Tao, Haizheng; Greaves, Neville G.; Richards, Tom; Lampronti, Giulio I.; Redfern, Simon A. T.; Blanc, Frédéric; Farha, Omar K.; Hupp, Joseph T.; Cheetham, Anthony K.; Keen, David A.

JACS

Melt-Quenched Glasses of Metal−Organic Frameworks

Thomas D. Bennett,[*,†] Yuanzheng Yue,[‡,§] Peng Li,[∥] Ang Qiao,[‡] Haizheng Tao,[‡] Neville G. Greaves,[†,‡,⊥] Tom Richards,[†] Giulio I. Lampronti,[#] Simon A. T. Redfern,[#] Frédéric Blanc,[∇] Omar K. Farha,[∥] Joseph T. Hupp,[∥] Anthony K. Cheetham,[†] and David A. Keen[○]

[†]Department of Materials Science and Metallurgy, University of Cambridge, 27 Charles Babbage Road, Cambridge CB3 0FS, United Kingdom

[‡]State Key Laboratory of Silicate Materials for Architectures, Wuhan University of Technology, Wuhan 430070, China

[§]Department of Chemistry and Bioscience, Aalborg University, DK-9220 Aalborg, Denmark

[∥]Department of Chemistry and International Institute for Nanotechnology, Northwestern University, Evanston, Illinois 60208, United States

[⊥]Institute of Mathematics, Physics and Computer Science, Aberystwyth University, Aberystwyth SY23 3BZ, United Kingdom

[#]Department of Earth Sciences, University of Cambridge, Downing Street, Cambridge CB2 3EQ, United Kingdom

[∇]Department of Chemistry and Stephenson Institute for Renewable Energy, University of Liverpool, Crown Street, Liverpool L69 7ZD, United Kingdom

[○]ISIS Facility, Rutherford Appleton Laboratory, Harwell Campus, Didcot, Oxon OX11 0QX, United Kingdom

S *Supporting Information*

ABSTRACT: Crystalline solids dominate the field of metal−organic frameworks (MOFs), with access to the liquid and glass states of matter usually prohibited by relatively low temperatures of thermal decomposition. In this work, we give due consideration to framework chemistry and topology to expand the phenomenon of the melting of 3D MOFs, linking crystal chemistry to framework melting temperature and kinetic fragility of the glass-forming liquids. Here we show that melting temperatures can be lowered by altering the chemistry of the crystalline MOF state, which provides a route to facilitate the melting of other MOFs. The glasses formed upon vitrification are chemically and structurally distinct from the three other existing categories of melt-quenched glasses (inorganic nonmetallic, organic, and metallic), and retain the basic metal−ligand connectivity of crystalline MOFs, which connects their mechanical properties to their starting chemical composition. The transfer of functionality from crystal to glass points toward new routes to tunable, functional hybrid glasses.
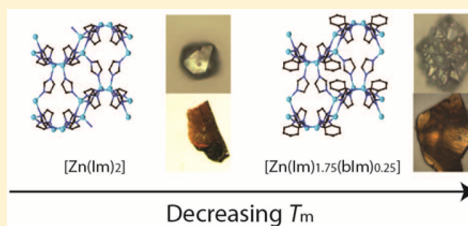
INTRODUCTION

The synthesis of crystalline metal−organic frameworks (MOFs) for gas sorption and separation, catalysis, drug delivery, conductive, and multiferroic applications is widespread.[1−4] These network materials consist of metal nodes linked by organic ligands in infinite arrays and are heralded for their chemical versatility in being able to accommodate an enormous range of ligand- or metal-based functionalities.[5−9] A family of MOFs known as zeolitic imidazolate frameworks (ZIFs) is of particular interest given their chemical stability and structural similarities to classical zeolite networks.[10,11] ZIFs have significantly softer mechanical properties compared to those of their inorganic cousins[12−14] and may structurally collapse upon heating, pressurization, or ball-milling[15] to form amorphous frameworks that possess the same short-range connectivity as that of their crystalline counterparts.[16]

Certain 1D and 2D coordination polymers exhibit transitions between solid and glasslike states[17,18] as does one 3D MOF, ZIF-4 [Zn(Im)$_2$] (Im = imidazolate, C$_3$H$_3$N$_2^−$).[19] These appear to be different from other melt-quenched glasses (MQGs), which are divided according to their underlying chemistry into inorganic nonmetallic (e.g., oxide and chalcogenide glasses), organic (e.g., polymer glasses), and metallic categories.[20] Importantly, the MQGs here are distinct from the sol−gel-derived hybrid amorphous solids reported by Novak,[21] which are produced via partial hydrolysis and subsequent condensation of metal alkoxides modified with an organic moiety (e.g., Si(OR)$_4$). Such MOF-glasses (our term for MQGs produced by quenching molten MOFs) form as a result of the freezing-in of the melt structure.

Motivated by the unique opportunities offered by transferring the chemical functionality of crystalline MOFs to thermo-mechanically stable glasses with tunable inorganic and organic components,[22] we present a detailed investigation of

the phenomenon of MOF melting in several 3D framework structures.

Pair distribution function (PDF) analysis, extended X-ray absorption fine structure (EXAFS), multinuclear solid-state nuclear magnetic resonance (NMR) spectroscopy, optical microscopy, differential scanning calorimetry (DSC), nano-indentation, and gas sorption analysis are used to investigate the relationship between four crystalline MOF structures and the properties of the related glasses. Importantly, we show that the melting temperature (T_m) of a MOF can be lowered by altering the chemistry of the crystalline state, and we use ^{13}C and ^{15}N NMR to shed light on the mechanism of melting. Furthermore, we identify differences between these glasses and amorphous (non-MQG) phases formed upon heating the crystalline structures below T_m. Although some display glasslike behavior, others do not and appear more closely associated with the solvent collapse of first-generation MOFs.[23]

The MOF-glasses formed upon heating above T_m and cooling maintain the extended framework connectivity reminiscent of the crystalline MOF state, though in a long-range disordered array. Variations in crystal chemistries lead to large differences in T_m, glass transition temperatures (T_g), and fragilities (m), alongside the elastic modulus (E) and hardness (H) of the glasses formed by quenching. By identifying common features in those MOFs that undergo melting and vitrification, we suggest new opportunities for the family that move away from the utilization of high surface areas.

■ RESULTS AND DISCUSSION

Materials Selection. An inter-related set of MOFs was chosen to separate the effects of chemistry and topology upon glass formation. ZIF-4 crystallizes in the orthorhombic space group *Pbca*, possessing a *cag* topology that is identical to the mineral variscite CaGa$_2$O$_4$ and includes eight nanopores per cell connected by apertures of 2.1 Å diameter (Figure 1a).[10] The structure is polymorphic with Zn(Im)$_2$ (GIS), a more open framework (porosity, P = 56.9%, compared to 23.6% for ZIF-4, Table 1) that adopts a different, gismondine network topology (Figure 1b) and crystallizes in space group $I4_1/a$.[11] The structure is not named in the literature. Mixed-ligand variants of ZIF-4 can be prepared using 5-methylbenzimidazolate (mbIm, C$_8$H$_7$N$_2$$^-$) or benzimidazolate (bIm, C$_7$H$_5$N$_2$$^-$), leading to compounds TIF-4 [Zn(Im)$_{1.5}$(mbIm)$_{0.5}$] and ZIF-62 [Zn(Im)$_{1.75}$(bIm)$_{0.25}$], which both adopt the same framework architecture and space group as those of ZIF-4 (Figures 1c,d and S1).[24,25]

Glass Transition and Melting Temperatures. In accordance with previous work, heating an evacuated sample of ZIF-4 results in structural collapse to an amorphous phase (termed a$_T$ZIF-4) at 600 K before recrystallization to a dense framework, ZIF-zni, just prior to melting at 863 K (Figures 1e and 2a).[16]

The Zn(Im)$_2$ (GIS) polymorph melts at a temperature almost identical to that of ZIF-4, after solvent loss in two stages at 400 and 475 K (Figure 2b). Upon heating in the DSC, TIF-4 undergoes solvent loss at a higher temperature of 525 K before melting at 740 K (Figure 2c). A partially evacuated sample of ZIF-62 (preheated at 440 K for 18 h, Figure S2) underwent the last stages of complete desolvation at 610 K (Figure 2d) before melting at 710 K (i.e., 30 K below the same point for TIF-4 and 150 K below ZIF-4).

The melting points are all clearly identified because the decomposition temperatures (T_d) in argon here are around 875
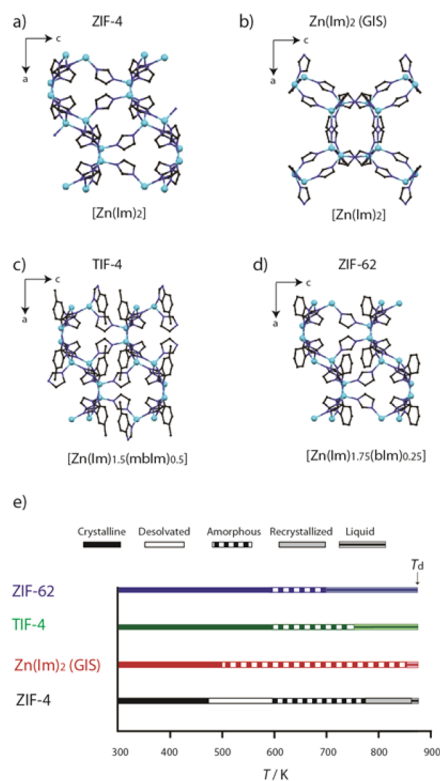
Figure 1. Unit cells viewed along the *b* axis of (a) ZIF-4, (b) Zn(Im)$_2$ (GIS), (c) TIF-4 and (d) ZIF-62. N, dark blue, Zn, light blue, C, black, and H, omitted. (e) Schematic of the thermal events on heating. Differences in behavior are evident, with Zn(Im)$_2$ (GIS), TIF-4, and ZIF-62 undergoing amorphization upon desolvation and a large temperature range between melting and framework decomposition for ZIF-62.

K (Figure S2a). However, the T_d of ZIFs is atmosphere-dependent,[26] and in air, the T_d values are ca. 673 and 713 K for TIF-4 and ZIF-62, respectively, thus precluding the melting process (Figure S3).

The decrease in melting point also provides insight into the mechanism. We previously inferred a reconstructive process upon melting and vitrification,[19] involving Zn−N bond breaking and reformation. This mechanism, based on the network topologies before and after melt-quenching and the relative weakness of the Zn−N bond within ZIF structures,[27] would be somewhat analogous to the description given by Kitagawa et al. of the melting in 1D zinc phosphate−imidazolate coordination polymers.[28] NMR data presented below provides supporting evidence in the observation of partially uncoordinated Im-based species in the recovered glasses.

Electron-donating groups attached to the imidazolate ring would be predicted to strengthen the Zn−N bond, given the soft−soft covalent interactions between the Zn^{2+} ion and Im-based ligands.[29] Indeed, the NMR data presented later in this work support this hypothesis, in terms of the increased electron density present on the nitrogen atoms in bIm and mbIm. However, here the addition of an electron donating benzene ring to the imidazolate anion is accompanied by a decrease in melting point (Table 1). Unfortunately calculation of individual bond strengths was precluded by the transition from crystalline to solvent-collapsed amorphous phase prior to melting, in the cases of Zn(Im)$_2$ (GIS), TIF-4, and ZIF-62.

Table 1. Compositions, Melting and Glass Transition Temperatures of the Glasses, and Liquid Fragilities and Crystalline Porosities

sample	composition	porosity (P) (%)[a]	melting point (K)	glass transition (K)	fragility (m)[b]
ZIF-4	$Zn(Im)_2$	23.6	863	565	39 (41)[19]
$Zn(Im)_2$ (GIS)	$Zn(Im)_2$	56.9	857	565 (560)	17 (15)
TIF-4	$Zn(Im)_{1.5}(mbIm)_{0.5}$	18.6	740	616	23
ZIF-62	$Zn(Im)_{1.75}(bIm)_{0.25}$	22.5	710	591	35

[a]Crystalline porosities calculated using the Mercury software with a probe radius of 1.2 Å and a grid spacing of 0.7 Å. [b]Fragilities of a_TZIF-4 and a_TZn(Im)$_2$ (GIS) and the glass transition temperature for a_TZn(Im)$_2$ (GIS) are italicized and in brackets where appropriate.
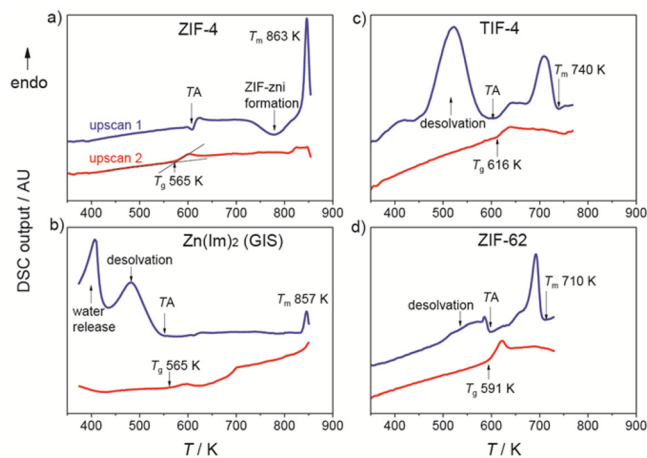
Figure 2. Enthalpic responses of the four samples on both the first (blue) and second (red) DSC heating upscans at 10 K/min. Thermal amorphization (T_A), water release, desolvation, crystallization, melting temperature (T_m), and glass transition temperature (T_g) are indicated. (a) ZIF-4 [Zn(Im)$_2$], (b) ZIF-GIS [Zn(Im)$_2$], (c) TIF-4 [Zn-(Im)$_{1.5}$(mbIm)$_{0.5}$], and (d) ZIF-62 [Zn(Im)$_{1.75}$(bIm)$_{0.25}$]. T_m refers to the offset temperature of the melting peak, whereas T_g is the onset temperature of glass transition peak. Initial endotherms related to solvent loss are not witnessed in the case of ZIF-4 because of prior structural evacuation. ZIF-62 was subjected to annealing at 440 K for 18 h prior to the DSC scanning, resulting in a smaller solvent release endotherm, associated with a mass loss of 0.55% (Figure S2).

Previous work has shown that recrystallization of ZIF-4 to ZIF-zni involves an increase in mean N−Zn−N and Zn−Im−Zn angles to closer to their ideal values (109.5 and 145°).[30] The inability of TIF-4 and ZIF-62 to support such changes (given the steric constraints placed upon the local coordination environment) may explain their lack of recrystallization to a dense phase prior to melting. This would be consistent with the higher melting temperature of ZIF-zni, compared to the amorphous phases of TIF-4 and ZIF-62 in which a distribution of values is expected. Some support is given to this latter statement by the greater distribution of N−Zn−N and Zn−Im−Zn angles, relative to those of ZIF-4 or ZIF-zni, in the amorphized sample of ZIF-4.[30]

The liquids formed in situ were cooled back to room temperature at 10 K/min, and glasses formed are referred to as a_gZIF-4, a_gZn(Im)$_2$ (GIS), a_gTIF-4, and a_gZIF-62. A second DSC heating scan was then carried out for all samples, which identified glass transition temperatures in each case (Figure 2a−d and Table 1).

The glass transition temperature was observed to increase upon addition of successively larger ligands to the MOF structures, from 565 K, in the case of a_gZIF-4 and a_gZn(Im)$_2$ (GIS), to 591 and 606 K for a_gZIF-62 and a_gTIF-4, respectively. The increase in T_g witnessed here for the series

of topologically identical MOFs is consistent with observations in many organic polymers,[31] where addition of bulky side groups is related to restriction of backbone motion and flexibility upon cooling of the liquid phase toward T_g.

Solvent Collapse and Glasslike Behavior. Variable temperature X-ray diffraction was used to probe the relationship between solvent removal and structural collapse (amorphization) in the samples. Successful solvent removal from the crystalline ZIF-4 structure has been reported previously, before a separate amorphization event. This amorphous structure, named a_TZIF-4, has been observed to possess a glass transition feature upon quenching and reheating.[19]

In contrast, solvent removal from Zn(Im)$_2$ (GIS) is associated with framework collapse (Figure S4) and formation of an X-ray amorphous material termed a_TZn(Im)$_2$ (GIS). This is consistent with the collapse of ZIF-6, a closely related framework, upon solvent removal.[32] Upon cooling to room temperature and reheating, a_TZn(Im)$_2$ (GIS) displays a glass transition (Figure S5), though unlike a_TZIF-4, no recrystallization is observed before melting at 857 K. Solvent release from TIF-4 also causes structural collapse and formation of an X-ray amorphous phase (Figure S4) termed a_TTIF-4 at 650 K (i.e., after the first solvent release endotherm). a_TTIF-4 was recovered to room temperature, and dissimilar to the glasslike a_TZIF-4 or a_TZn(Im)$_2$ (GIS), did not show any T_g-like features upon rescanning in the DSC (Figure S6a).

Investigation into a_TZIF-62 also failed to find any glasslike behavior (Figure S6b), providing clear evidence for differences in amorphous (non-melt-quenched) and MQG phases. This sequence of phase transitions helps explain the relative sharpness of the observed DSC melting peaks. The peak is relatively sharp in the heating scan of ZIF-4 (i.e., the melting of ZIF-zni), which implies that the crystals are uniform.

The peak obtained because of the melting of ZIF-GIS is however slightly broader, though it also appears smaller in intensity because of the far larger desolvation enthalpies recognized from this more porous system. The melting peaks observed upon the heating scans of TIF-4 and ZIF-62 are broader still, though this is ascribed to melting of the amorphous (non MQG) phases, and reflects some degree of structural heterogeneity.

Fragility Measurements. The fictive temperature, T_f, of a glass (i.e., in the nonliquid state) may be thought of as the temperature at which the structure of an equilibrium liquid is frozen in.[33] The dependence of T_f upon the heating rate used in the DSC scan (q_h) (Figure S5) allows determination of the kinetic fragility index, m,[19,33,34] which quantifies the speed of the dynamical processes of a liquid as it approaches the glass transition temperature. Interestingly, despite ZIF-4 and Zn-(Im)$_2$ (GIS) possessing the same chemical formula and melting at the same temperature, the thus-produced liquids exhibit very

different fragilities ($m = 39$ and 17 respectively, Figure 3). The differences here were confirmed by evaluation of m for
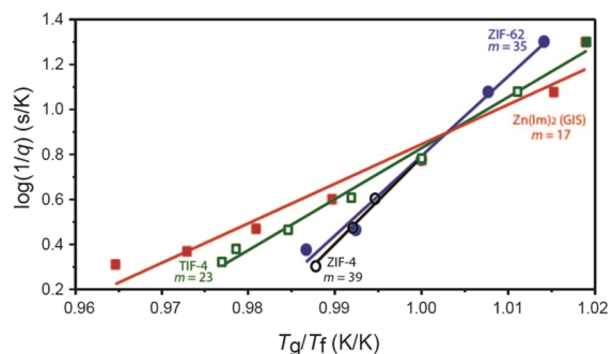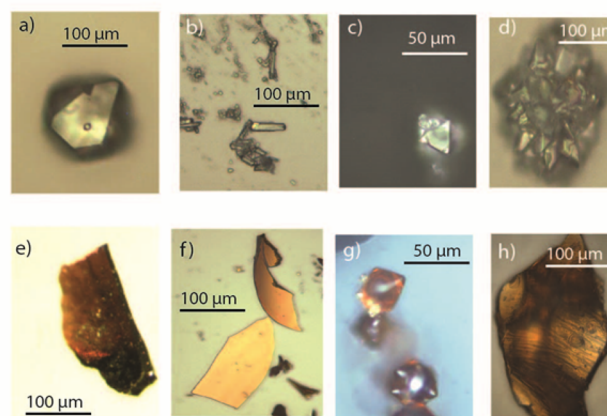

Figure 3. Fragilities of ZIF-4, Zn(Im)$_2$ (GIS), TIF-4, and ZIF-62, determined from the dependence of fictive temperature (T_f) on the heating rate (q_h) by using the DSC method. Large values of m may indicate fragile liquids that form relatively ductile glasses (e.g., toluene, $m = 105$), whereas lower fragilities have been suggested to characterize strong liquids that vitrify to yield brittle glasses (e.g., silica, $m = 20$).[36−38] Black open circles, ZIF-4, red squares, Zn(Im)$_2$ (GIS), green open squares, TIF-4, and blue closed cirlces, ZIF-62.

a_TZn(Im)$_2$ (GIS) ($m = 15$), which lies close to that of a_gZn(Im)$_2$ (GIS) (Figure S7). This is consistent with the noticeably similar fragilities of a_gZIF-4 ($m = 39$) and a_TZIF-4 ($m = 41$).

The different fragilities of the liquids formed upon melting of ZIF-4 and Zn(Im)$_2$ (GIS) may stem from a remnant influence of the network architecture of the solid phase, given the relatively small window between melting and quenching of the samples. Indeed, although chemically identical, the phases immediately prior to melting are not the same (ZIF-zni and a_TZn(Im)$_2$ (GIS), respectively). Fragility was also observed to decrease on going from ZIF-4 ($m = 39$) to ZIF-62 ($m = 35$) and then to TIF-4 ($m = 23$); hence, for those frameworks displaying the *cag* topology, fragility decreases with increasing linker content and size.

Although an increase in fragility with increasing linker size may have been expected on the basis of free volume considerations and the increase in T_g, similar changes in the fragility index of other glass-forming polymers have been noted[31,35] and ascribed to the relative side group stiffness compared to that of the polymer backbone. The lower kinetic fragilities of the Zn(Im)$_2$ (GIS) and TIF-4 melts compared to that of the ZIF-4 melt are consistent with smaller C_p increases during the glass transition, given that the latter is a measure of thermodynamic fragility.[20]

Pair Distribution Function and X-ray Absorption Fine-Structure Measurements. Bulk samples of each crystalline phase were subsequently heated in a tube furnace under flowing argon to 863 K (ZIF-4), 857 K (Zn(Im)$_2$ (GIS)), 740 K (TIF-4), and 710 K (ZIF-62) (i.e., above the respective melting endotherms but before thermal decomposition). Cooling of the samples under argon yielded X-ray-amorphous products (Figure S1), with vitrification resulting in remarkable morphological changes (Figure 4). All single crystals show appreciable flow during vitrification, whereas the needle structures of Zn(Im)$_2$ (GIS) undergo macroscopic changes into sheetlike glasses of a_gZn(Im)$_2$ (GIS). Micrographs of these glasses under parallel and crossed-polarized light are reported in Figure S8, confirming optical isotropy.


Figure 4. (a−d) Optical images of crystalline samples of ZIF-4, Zn(Im)$_2$ (GIS), TIF-4, and ZIF-62. The products formed upon melting and quenching (e−h) clearly resemble glasses formed from macroscopic flow.

Elemental analysis revealed few differences between crystalline and vitrified phases, aside from those associated with the loss of solvent (section SI-4), whereas they demonstrated no uptake of N$_2$ gas during sorption measurements (Table S1). Ultraviolet−visible (UV−vis) spectroscopy carried out on the crystalline samples showed the expected bathochromic shift in the position of λ_{max} from those samples incorporating the Im linker (ZIF-4 and Zn(Im)$_2$ (GIS)) to those with bIm and mbIm organics (TIF-4 and ZIF-62). In the latter two cases, absorption bands were also much broader. On vitrification, few distinguishable absorption bands were recorded (Figure S9). Curiously, although Raman spectroscopy also demonstrated similarities between crystalline phases (Figure S10) and yielded little information on a_gZIF-4, a_gZn(Im)$_2$ (GIS), or a_gTIF-4 because of their nontransparent nature, the spectrum of a_gZIF-62 contained features extremely similar to those of the crystalline framework.

Diffuse reflectance infrared spectroscopy (DRIFTS) was also carried out on the samples (Figure S11). In all cases, spectra of the crystalline MOF and its corresponding glass were largely similar, though are dominated by contributions from the imidazole-based rings. Merging of bands associated with stretching of the aromatic organic rings was observed in the glass phases.

EXAFS was carried out on both crystalline and vitrified samples in order to provide information on the first zinc coordination shell and to determine whether the tetrahedral configuration was maintained in the glass phase. Data extracted through Fourier transformation of the X-ray absorption spectra are similar between crystal and corresponding glasses (Figure 5). In particular, all spectra exhibit one strong peak at ca. 1.6 Å. Comparison with other EXAFS data on ZIFs, which were also not phase-shift-corrected, confirm that this feature corresponds to the zinc−nitrogen distance of 2 Å.[39] This peak is invariant in both position and intensity upon vitrification and confirms that the local environment of Zn^{2+} ions is identical in the glasses (i.e., each is coordinated by four nitrogen atoms in a tetrahedral environment). Further similarities between crystal and glass to 4 Å are expected given that this limit represents the distance to the second N donor atom on the rigid, planar imidazolate ligand.
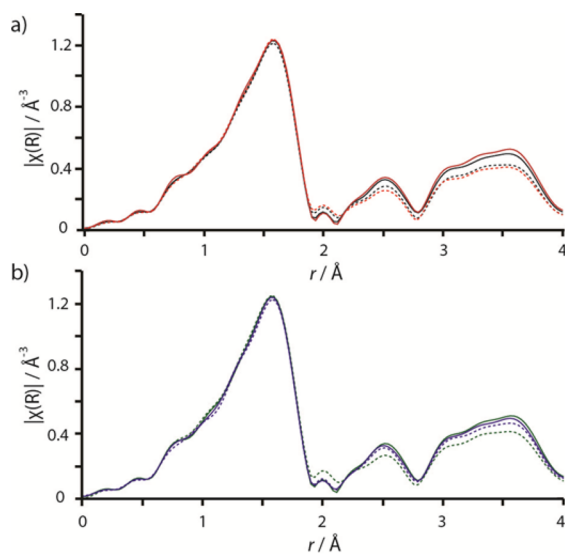
Figure 5. Pseudoradial distribution functions for crystalline (solid lines) and vitrified (broken lines) samples of (a) ZIF-4 and $Zn(Im)_2$ (GIS) and (b) TIF-4 and ZIF-62. Data were extracted through Fourier transformation of the X-ray absorption spectra (Figure S12), obtained at the K edge of zinc. Phase-shift corrections were not applied. Black, ZIF-4, red, $Zn(Im)_2$ (GIS), green, TIF-4, and blue, ZIF-62.

Given recent advances in the study of disordered MOFs by PDF methods,[40−42] the detailed chemical structures of all samples here were probed by collecting room-temperature X-ray total scattering data (Ag source, $\lambda = 0.561$ Å, $Q_{max} = 20$ Å^{-1}). The resultant, near-identical structure factors $S(Q)$ (Figure S13) of the vitrified materials confirm their amorphous nature. Subsequent Fourier transform yields the PDFs $D(r)$, though modeling was not attempted because of insufficient data quality.

Although the crystalline sample PDFs contain long-range oscillations attributed to their crystallographic order on length scales exceeding 20 Å (Figure 6a), those of the glasses are essentially featureless above 8 Å (Figure 6b). Below this distance, all eight PDF traces are virtually identical, with only small differences in peak intensities. They also display a remarkable similarity to those of ZIFs amorphized by ball-milling and at lower temperatures (prior to recrystallization and melting).[43] Assignment of the five physical sharp features below 6 Å was carried out by using the PDFGUI software to calculate the partial PDFs for the constituent atom pairs of ZIF-4 (Figure S14).[10,44] (The first peak at 0.74 Å is considered an artifact because it is typically very difficult to obtain reliable data below ∼1Å from lab-based X-ray total scattering instruments.)

The first real feature at 1.3 Å corresponds to C−C or C−N aromatic linkages within the imidazolate ring, whereas the more intense peak at 2 Å indicates nearest-neighbor Zn and N atoms, importantly confirming the retention of metal−organic association in the glass phases. Zn−N distances also account for the peak at 4.1 Å, though this is the distance between metal centers and the second N atom in the organic ligand. These two features are separated by a peak at 3 Å, due to correlations between nearest neighbor Zn and C atoms.

At longer distances, all PDFs are dominated by scattering from Zn due to its larger scattering cross section relative to those of C, N, and H. The last intense peak in the spectra of the glasses occurs at 6 Å and belongs to nearest zinc atom neighbors. This limit of short-range order is consistent with
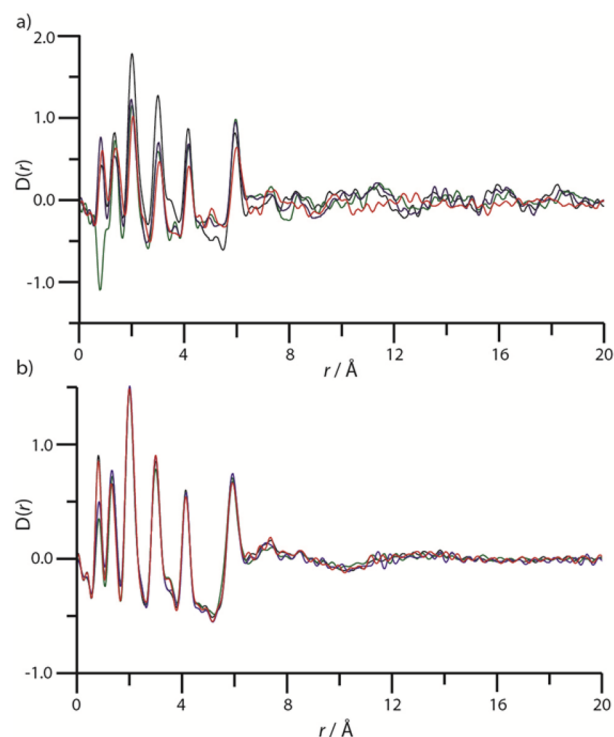

Figure 6. (a) Pair distribution function $D(r)$ calculated via Fourier transform of the X-ray total scattering function $S(Q)$ for ZIF-4 (black), $Zn(Im)_2$ (GIS) (red), TIF-4 (green), and ZIF-62 (blue). (b) Pair distribution function $D(r)$ calculated via Fourier transform of the X-ray total scattering function $S(Q)$ for a_gZIF-4 (black), a_gZn(Im)$_2$ (GIS) (red), a_gTIF-4 (green), and a_gZIF-62 (blue).

prior reports of amorphous ZIFs and the retention of metal−organic−metal connectivity.[43] This is consistent with PDF studies of silica glass,[45] where the local tetrahedral coordination and order around Si centers is preserved to 3.1 Å, though framework order is lost. The longer distance associated with this local order in ZIFs is due to the larger bridging ligand ($C_3H_3N_2^-$ compared to O). The similarities of the PDFs of crystalline TIF-4 and ZIF-62 to that of ZIF-4 is due to the negligible effect on the PDFs of additional contributions from the extra aromatic carbon atoms of the benzene rings in the structures of TIF-4 and ZIF-62.

A smaller, slightly broader peak centered at 7 Å is visible in the PDFs of the glasses. This distance is populated by Zn−C and Zn−N correlations in the partial PDFs of ZIF-4, where both nonmetal atoms are located on the second-nearest imidazolate ion to the metal center. It is possible, though not confirmed, that this small feature suggests that a Zn−Im−Zn−Im motif is present in all glasses and provides possible evidence of order extending beyond Zn−Im−Zn correlations.

Solid-State Nuclear Magnetic Resonance Data. The ^{13}C and ^{15}N cross-polarization (CP) magic angle spinning (MAS) solid-state NMR spectra of the crystalline samples show most of the individual carbon and nitrogen atoms in the asymmetric unit cell (Figure 7a). Differences in the ^{13}C and ^{15}N spectra of crystalline ZIF-4[46] and $Zn(Im)_2$ (GIS) are reflective of the different number of crystallographically independent ligands (4 cf. 16), whereas additional resonances at 162.1 ppm, 42−12 ppm (in the ^{13}C NMR), and 133 ppm (in the ^{15}N NMR) correspond to diethylformamide inside the pores of Zn(Im)2 (GIS) (section SI-9).
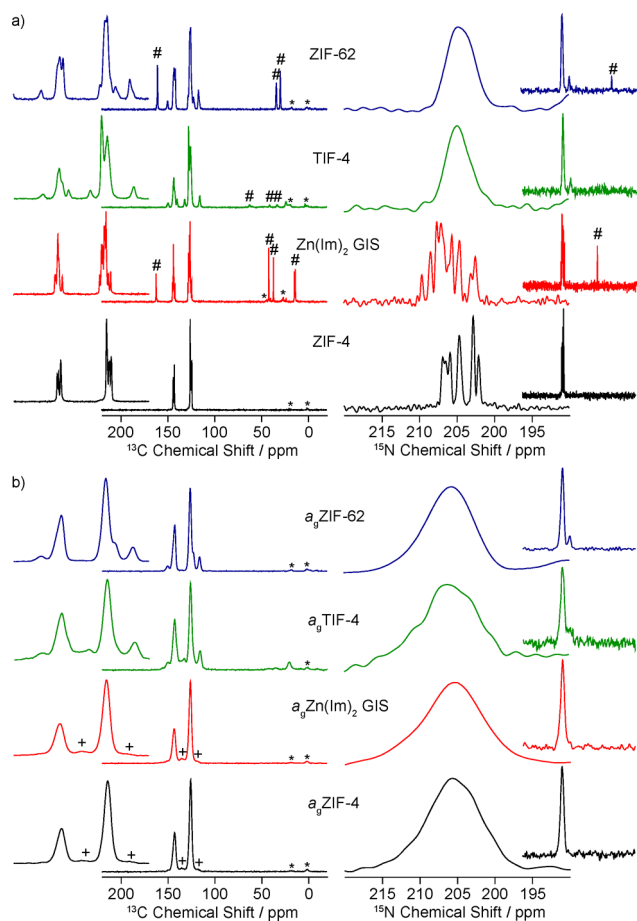
Figure 7. ^{13}C (left) and ^{15}N (right) CP MAS NMR spectra of (a) ZIF-4 (black), Zn(Im)$_2$ (GIS) (red), TIF-4 (green), and ZIF-62 (blue), and (b) the corresponding glass phases of a_gZIF-4, a_gZn(Im)$_2$ (GIS), a_gTIF-4, and a_gZIF-62 obtained at 9.4 T. Spinning sidebands are marked with asterisks (*), decoordinated Im ligands are marked with plus signs (+), and adsorbed residual solvent synthesis are marked with pound signs (#). ^{13}C insets show magnified views of the 160−110 ppm region, whereas the ^{15}N inset shows a wider 290−50 ppm view. Proposed spectral assignments are given in Tables S3 and S4.

Additional ^{13}C resonances in the spectra of TIF-4 and ZIF-62 are assigned to mbIm or bIm ligands. (See Table S3 for complete assignments.) Notably, the presence of these linkers was also confirmed by two additional resonances in the ^{15}N spectra of TIF-4 and ZIF-62, the smaller shift observed for the bIm/mbIm ligands (190.2/188.8 ppm) versus the Im ligands (205.2 ppm) reflecting the slightly larger shielding effect of the benzimidazolate group.[47]

All individual resonances in the ^{13}C and ^{15}N CP MAS NMR spectra of a_gZIF-4, a_gZn(Im)$_2$ (GIS), a_gTIF-4, and a_gZIF-62 glasses (Figure 7b) are much broader than those for the corresponding crystalline materials, and this is consistent with the existence of amorphous phases, as noted previously.[46] Importantly, the NMR results of these materials confirm that the organic linkers remain intact in the vitrified products, as previously observed in other amorphous ZIFs prepared by mechanosynthesis.[46] (See Table S4 for spectral assignments.) The solvent signals observed in the crystalline phases have disappeared, in agreement with the solvent removal observed by DSC.

Both ^{13}C and ^{15}N NMR spectra of a_gZIF-4 and a_gZn(Im)$_2$ (GIS) are virtually identical with the NCN and NCC carbons

and CNC nitrogens of the Im ligand appearing at the same chemical shift (Table S4). Two additional small resonances are also observed and are assigned to uncoordinated imidazole on the basis of known chemical shifts.[46] Such differences between crystal and glasses were not identifiable in the PDF measurements. Similar partial decoordination of 2-methylimidazolate was previously observed in amorphous ZIF-8 (prepared by ball-milling) but not of unsubstituted imidazolate, as in amorphous ZIF-4 and ZIF-zni,[46] suggesting that melt-quenching is a more energy-rich process than milling.

Although at first sight the NMR data obtained on the mixed-ligand glasses a_gTIF-4 and a_gZIF-62 appear relatively similar with the observation of the Im ligands (at 142 and 126 ppm for NCN and NCC carbons and at 206 for CNC nitrogen) and the benzimidazole moieties (at 145−150 and 116 ppm for the NCN and CHCN and at 190 ppm for CNC), close inspection of the ^{13}C spectra reveals differences and the identification of both the mbIm linker in a_gTIF-4 and the bIm moieties in a_gZIF-62. Specifically, the ^{13}C NMR fingerprints of mbIm are clearly seen in Figure 7b with the observation of the CHCHCN (140 ppm), CCH$_3$CHCN (132 ppm), and CH$_3$ carbons (21 ppm), the bIm ligand gives rise to a signal at 123 ppm typical of the CHCHCN carbon. We note that in spite of the fact that we could not detect free imidazole or (5-methyl)benzimidazole because of their overlapping resonances with the ones of a_gTIF-4 and a_gZIF-62 it is likely that some ligand decoordination process also occurs.

Mechanical Properties and Densities. The densities of the crystalline materials, the amorphous (non-MQG) phases, and the melt-quenched glasses themselves were probed using gas pycnometry. The densities of the dense ZIF-zni phase (for ZIF-4) and the amorphous phases formed prior to melting (for Zn(Im)$_2$ (GIS), TIF-4 and ZIF-62) were all higher than those of the initial crystalline frameworks (Table S2). This is unsurprising, given the collapse of other porous crystals such as ZrW$_2$O$_8$ and silicalite.[48,49] Density changes from these phases to the melt-quenched glasses were much less significant, though still involved an increase. The sample with the lowest T_m, ZIF-62, gave rise to the least dense glass in the study, though curiously we observed an increase in density of the glass formed by quenching the liquid from 845 K (cf. just above T_m).

The mechanical properties of TIF-4, along with those of a_gZIF-4, a_gZn(Im)$_2$ (GIS), a_gTIF-4, and a_gZIF-62, were probed by nanoindentation on suitable single crystals or monoliths. E, the elastic modulus, measures the ease of deformation along one axis of a material and, as such, has been used as a measure of MOF stiffness. Hardness, H, indicates the resistance to plastic deformation of a material, though it is heavily dependent upon experimental parameters.[50] Values of E and H are included in Table S5.

Analysis of the load-displacement data (Figure S15) revealed the anisotropic elastic modulus of TIF-4 ($E_{111} \approx 6.4$ GPa) to be significantly greater than the corresponding value for ZIF-4 ($E_{111} \approx 4.7$ GPa) reported in a previous study,[16] which is consistent with the higher density of TIF-4 and may be ascribed to the larger organic present. Upon vitrification to a_gTIF-4, significant stiffening is observed ($E \approx 7.9$ GPa), which reflects an increase in pycnometric density. Indeed, the elastic moduli of the glasses correlate well with their pycnometric densities (Figure 8), whereas those of identical chemical composition possess comparative elastic moduli.

The large temperature range between T_m and T_d in ZIF-62 allowed heating to 845 K (i.e., 135 K above T_m), without
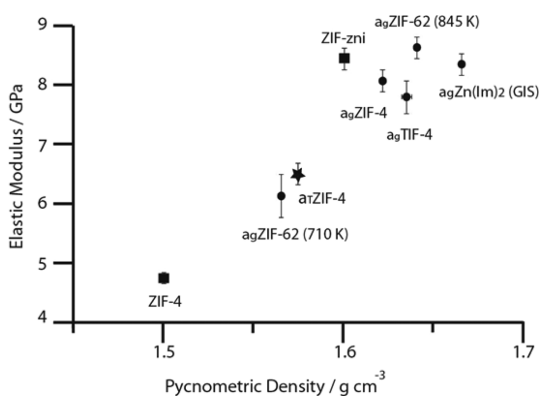
Figure 8. Correlation between elastic modulus and physical density of the melt-quenched glasses, temperature-amorphized ZIF-4, and the crystalline ZIF-4 and ZIF-zni.

framework decomposition. This sample was vitrified upon cooling and found to exhibit a significantly larger elastic modulus compared to that of the sample cooled from just above T_m ($E \approx 8.8$ GPa, Figure S15). This increase in rigidity is expected, given the similar density of the sample compared to that of others in the study, and suggests a better structural equilibration of the glass formed from a higher temperature melt, despite the identical cooling rates used. In analogous fashion, an increase (ca. 33%) in hardness was also noted. Interestingly however, H was invariant between TIF-4 and a_gTIF-4 (Figure S16). All H values were observed to lie in the range of 0.2–1.5 GPa, which is in agreement with previously determined H values for MOFs.

CONCLUSIONS

The melting point of a MOF was manipulated by altering the chemical composition of the crystalline framework prior to melting. This approach, in which T_m can be lowered by the addition of varying quantities of larger organic ligands, provides routes to achieve generalization of the phenomenon and achieves melting in MOFs that do not obey the currently necessary $T_m < T_d$ condition. The mechanism involves partial linker decoordination; thus, the melting temperature is expected to be partially dependent upon the metal–ligand bond strength. Sterically bulky species are observed to decrease the melting point, whereas structural anisotropy allows melting instead of thermal decomposition (i.e., simultaneous decoordination of all metal–ligand bonds).

Alongside reducing T_m, the introduction of successively larger organic ligands into topologically identical frameworks decreases the fragilities of the glass forming liquids. The effect of framework architecture upon melting temperature however appears less clear, with identical values of T_m reported across chemically identical, topologically distinct systems. In this latter case, the fragility index is however very different, which may suggest a topological contribution to the melting process.

The effect of increasing the size of organic ligand upon elastic moduli of the glasses formed can also be predicted. Rationalized in terms of packing ability, the decrease in elastic moduli upon increasing the size of the organic component presented here is reminiscent of work on hybrid organic–inorganic sol gels[51] and points toward significant analogies between these materials and MOF-glasses. The striking result of an increase in E upon quenching of the liquid formed from heating ZIF-62 above T_m merits further investigation.

The demonstration of the melting of several 3D MOFs has important consequences for the growing list of potential applications for this burgeoning class of materials. First and foremost, melting opens up new routes to hybrid glasses, the chemical functionality of which may be altered by utilizing the chemical versatility of the crystalline MOF state. Through this work, we expect that the family of MOF-glasses (i.e., a new type of MQG) can be expanded for various applications (e.g., in advanced photonics and lighting). Alongside the glasses themselves, in situ formation from liquids will prove of great interest in producing precise, desired morphologies via melt-casting or -spinning processes. However, this new area of MOF research leads to questions such as the nature of the liquids produced,[52] the effect of quenching rate upon mechanical properties, and the predictability of the phenomenon.

■ EXPERIMENTAL SECTION

Synthesis. Microcrystalline powders of the four crystalline MOFs were synthesized using established methodology (Figures S1 and S2).[11,24,25,53]

Differential Scanning Calorimetry. DSC experiments were carried out using a Netzsch STA 449 F1 instrument in an inert argon atmosphere. The samples were placed in a platinum crucible situated on a sample holder of the DSC at room temperature and subjected to varying numbers of up- and downscans, depending on the purpose of the measurements. After natural cooling to room temperature, the subsequent upscans were carried out using the same procedure as for the first. Using DSC, we determined the fictive temperature as a function of the up- and downscan rate. On the basis of the heating rate dependence of fictive temperature, liquid fragility indices were evaluated according to previous literature.[19]

Gas Pycnometry and N$_2$ Sorption. Pycnometric measurements were carried out using a Micromeritics Accupyc 1340 helium pycnometer. The typical mass used was 200 mg; the values quoted are the mean and standard deviation from a cycle of 10 measurements. N$_2$ sorption isotherm measurements were carried out on a Micromeritics Tristar II 3020 (Micromeritics, Norcross, GA) at 77K. Between 80 and 100 mg of material was used for each measurement. Surface areas were estimated by applying the Brunauer–Emmett–Teller (BET) equation.

X-ray Diffraction. Room-temperature powder X-ray diffraction (PXRD) data ($2\theta = 5–30°$) were collected with a Bruker-AXS D8 diffractometer using Cu Kα ($\lambda = 1.540598$ Å) radiation and a LynxEye position-sensitive detector in Bragg–Brentano parafocusing geometry. Variable-temperature PXRD data were collected in Bragg–Brentano geometry with a Bruker-AXS D8 diffractometer equipped with primary Gobbel mirrors for parallel Cu Kα X-rays, a Vantec position-sensitive detector, and an MRI heating stage. Collections conditions were: 3–30° in 2θ, 0.02 step size, 100 s/step, and divergence slit 0.6 mm. X-ray total scattering data were collected at room temperature on the crystalline and a_m-ZIFs using a PANalytical Ag-source X'pert Pro MPD lab diffractometer ($\lambda = 0.561$ Å). Data collection was carried out using loaded 1.0 mm diameter quartz capillaries and collection times of approximately 18 h. Corrections for background, multiple scattering, container scattering, and absorption were applied using the GudrunX program.[54−56]

Nanoindentation. The Young's modulus (E) of the samples was measured using an MTS Nanoindenter XP at ambient conditions. The Miller indices of single crystals of TIF-4 were predicted using the Mercury software.[57] Samples were mounted in an epoxy resin and polished using increasingly fine diamond suspensions. Indentation experiments were carried out under the dynamic displacement controlled mode at a constant strain rate of 0.05 s^{-1}. All tests were conducted using a three-sided pyramidal (Berkovich) diamond indenter tip to a maximum surface penetration depth of 500 nm. The load-displacement data collected were analyzed using the Oliver & Pharr method.[58] A Poisson's ratio of 0.2 was used, in accordance with prior studies on ZIF materials.[12]

Raman Spectroscopy. The Raman spectra were measured with a LabRAM HR Evolution HORIBA Scientific instrument equipped with an Olympus 100× microscope objective. The measurements were carried out at room temperature in the range $100-4000$ cm^{-1} with 10 accumulation scans and 2 s acquisition time.

Diffuse Reflectance Infrared and UV–Visible Spectroscopy. Diffuse reflectance infrared spectra (DRIFTS) were recorded on a Nicolet 7600 FTIR spectrometer equipped with an MCT detector. The spectra were collected in a KBr mixture under N_2 purge using KBr as the background. UV–vis diffuse-reflectance spectra were collected at room temperature using a Shimadzu UV-3600 PC double-beam, double-monochromator spectrophotometer operating from 200 to 800 nm. $BaSO_4$ was used as a nonabsorbing reflectance reference.

Polarized Light Microscopy. All materials were studied with a Zeiss Axioplan and Canon A630 polarized-light petrographic photo-microscope.

Extended X-ray Absorption Fine-Structure Spectroscopy. X-ray absorption spectra were collected in transmission mode on Beamline B18 at the Diamond light source (DLS) operating in a 10 min top-up mode for a ring current of 200 mA and an energy of 3 GeV. The radiation was monochromated with a Si(111) double crystal, and harmonic rejection was achieved through the use of two platinum-coated mirrors operating at an incidence angle of 6.0 mrad. The monochromator was calibrated using the K-edge of a Zn foil, taking the first inflection point in the Zn edge as 9659 eV. Three scans of each sample were taken, aligned using data taken on Zn foil reference, and subsequently averaged. The Athena software program was used for data processing. Data in the range $3 < k < 15$ Å^{-1} were Fourier transformed and k^2 weighted. Phase-shift corrections were not applied.

Solid-State NMR Spectroscopy. All solid-state NMR measurements were carried out on a 9.4 T Bruker Avance III HD NMR spectrometer equipped with a 4 mm HXY triple-resonance MAS probe at ^{1}H Larmor frequency of 400.13 MHz with the X and Y channels tuned to ^{13}C and ^{15}N at 100.63 and 40.55 MHz, respectively. All NMR spectra were obtained with CP at MAS frequencies of 12.5 kHz and 10 kHz for ^{13}C and ^{15}N, respectively. ^{1}H pulses and SPINAL-64 heteronuclear decoupling[59] were carried out at a radio frequency (rf) field amplitude of 83 kHz. ^{13}C CP MAS experiments were obtained with optimized contact times of 2 ms and with a ^{13}C rf field of 40 kHz, whereas the ^{1}H rf field amplitude was ramped to obtain maximum signal at a ^{1}H rf field of approximately 60 kHz. ^{15}N CP MAS experiments were obtained with contact times of 5 ms and with a ^{15}N rf field of 33 kHz, whereas the ^{1}H rf field amplitude was ramped to obtain maximum signal at a ^{1}H rf field of approximately 40 kHz. ^{13}C and ^{15}N chemical shifts (± 0.2 and ± 1 ppm for the crystalline and glasses materials, respectively) were externally referenced to the CH_3 group of alanine at 20.5 ppm (corresponding to the CH group of adamantane at 29.45 ppm)[60] and the NH_3^+ group of glycine at 33.4 ppm (corresponding to liquid NH_3 at 0 ppm).[61] All samples were packed in air.

ASSOCIATED CONTENT

Ⓢ Supporting Information

The Supporting Information is available free of charge on the ACS Publications website at DOI: 10.1021/jacs.5b13220.

> PXRD, TGA, DSC, elemental analysis, gas sorption, EXAFS, total scattering, full NMR spectral assignments, and nanoindentation data. (PDF)

AUTHOR INFORMATION

Corresponding Author

*tdb35@cam.ac.uk

Notes

The authors declare no competing financial interest.

REFERENCES

(1) Furukawa, H.; Cordova, K. E.; O'Keeffe, M.; Yaghi, O. M. *Science* **2013**, *341*, 974.

(2) Nugent, P.; Belmabkhout, Y.; Burd, S. D.; Cairns, A. J.; Luebke, R.; Forrest, K.; Pham, T.; Ma, S. Q.; Space, B.; Wojtas, L.; Eddaoudi, M.; Zaworotko, M. J. *Nature* **2013**, *495*, 80.

(3) Shimizu, G. K. H.; Taylor, J.; Kim, S. *Science* **2013**, *341*, 354.

(4) Jain, P.; Ramachandran, V.; Clark, R. J.; Zhou, H. D.; Toby, B. H.; Dalal, N. S.; Kroto, H. W.; Cheetham, A. K. *J. Am. Chem. Soc.* **2009**, *131*, 13625.

(5) Stock, N.; Biswas, S. *Chem. Rev.* **2012**, *112*, 933.

(6) Morris, R. E.; Cejka, J. *Nat. Chem.* **2015**, *7*, 381.

(7) Allendorf, M. D.; Stavila, V. *CrystEngComm* **2015**, *17*, 229.

(8) Guillerm, V.; Ragon, F.; Dan-Hardi, M.; Devic, T.; Vishnuvarthan, M.; Campo, B.; Vimont, A.; Clet, G.; Yang, Q.; Maurin, G.; Férey, G.; Vittadini, A.; Gross, S.; Serre, C. *Angew. Chem., Int. Ed.* **2012**, *51*, 9267.

(9) McDonald, T. M.; Mason, J. A.; Kong, X. Q.; Bloch, E. D.; Gygi, D.; Dani, A.; Crocella, V.; Giordanino, F.; Odoh, S. O.; Drisdell, W. S.; Vlaisavljevich, B.; Dzubak, A. L.; Poloni, R.; Schnell, S. K.; Planas, N.; Lee, K.; Pascal, T.; Wan, L. W. F.; Prendergast, D.; Neaton, J. B.; Smit, B.; Kortright, J. B.; Gagliardi, L.; Bordiga, S.; Reimer, J. A.; Long, J. R. *Nature* **2015**, *519*, 303.

(10) Park, K. S.; Ni, Z.; Cote, A. P.; Choi, J. Y.; Huang, R. D.; Uribe-Romo, F. J.; Chae, H. K.; O'Keeffe, M.; Yaghi, O. M. *Proc. Natl. Acad. Sci. U. S. A.* **2006**, *103*, 10186.

(11) Tian, Y. Q.; Zhao, Y. M.; Chen, Z. X.; Zhang, G. N.; Weng, L. H.; Zhao, D. Y. *Chem. - Eur. J.* **2007**, *13*, 4146.

(12) Tan, J. C.; Bennett, T. D.; Cheetham, A. K. *Proc. Natl. Acad. Sci. U. S. A.* **2010**, *107*, 9938.

(13) Horike, S.; Shimomura, S.; Kitagawa, S. *Nat. Chem.* **2009**, *1*, 695.

(14) Schneemann, A.; Bon, V.; Schwedler, I.; Senkovska, I.; Kaskel, S.; Fischer, R. A. *Chem. Soc. Rev.* **2014**, *43*, 6062.

(15) James, S. L.; Friscic, T. *Chem. Soc. Rev.* **2013**, *42*, 7494.

(16) Bennett, T. D.; Goodwin, A. L.; Dove, M. T.; Keen, D. A.; Tucker, M. G.; Barney, E. R.; Soper, A. K.; Bithell, E. G.; Tan, J. C.; Cheetham, A. K. *Phys. Rev. Lett.* **2010**, *104*, 115503.

(17) Chen, W.; Horike, S.; Inukai, M.; Kitagawa, S. *Polym. J.* **2015**, *47*, 141.

(18) Umeyama, D.; Horike, S.; Inukai, M.; Itakura, T.; Kitagawa, S. *J. Am. Chem. Soc.* **2015**, *137*, 864.

(19) Bennett, T. D.; Tan, J. C.; Yue, Y. Z.; Baxter, E.; Ducati, C. D.; Terrill, N.; Yeung, H. Y.; Zhou, Z.; Chen, W.; Henke, S.; Cheetham, A. K.; Greaves, G. N. *Nat. Commun.* **2015**, *6*, 8079.

(20) Angell, C. A. *Science* **1995**, *267*, 1924.

(21) Novak, B. M. *Adv. Mater.* **1993**, *5*, 422.

(22) Vendamme, R.; Onoue, S. Y.; Nakao, A.; Kunitake, T. *Nat. Mater.* **2006**, *5*, 494.

(23) Kitagawa, S.; Kondo, M. *Bull. Chem. Soc. Jpn.* **1998**, *71*, 1739.

(24) Gustafsson, M.; Zou, X. D. *J. Porous Mater.* **2013**, *20*, 55.

(25) Wu, T.; Bu, X. H.; Zhang, J.; Feng, P. Y. *Chem. Mater.* **2008**, *20*, 7377.

(26) Yin, H.; Kim, H.; Choi, J.; Yip, A. C. K. *Chem. Eng. J.* **2015**, *278*, 293.

(27) Gadipelli, S.; Travis, W.; Zhou, W.; Guo, Z. *Energy Environ. Sci.* **2014**, *7*, 2232.

(28) Horike, S.; Chen, W.; Itakura, T.; Inukai, M.; Umeyama, D.; Asakura, H.; Kitagawa, S. *Chem. Commun.* **2014**, *50*, 10241.

(29) Boussouf, K.; Boulmene, R.; Prakash, M.; Komiha, N.; Taleb, M.; Mogren Al-Mogren, M. M.; Hochlaf, M. *Phys. Chem. Chem. Phys.* **2015**, *17*, 14417.

(30) Beake, E. O.; Dove, M. T.; Phillips, A. E.; Keen, D. A.; Tucker, M. G.; Goodwin, A. L.; Bennett, T. D.; Cheetham, A. K. *J. Phys.: Condens. Matter* **2013**, *25*, 395403.

(31) Kunal, K.; Robertson, C. G.; Pawlus, S.; Hahn, S. F.; Sokolov, A. P. *Macromolecules* **2008**, *41*, 7232.

(32) Bouëssel du Bourg, L. B.; Ortiz, A. U.; Boutin, A.; Coudert, F. X. *APL Mater.* **2014**, *2*, 124110.

(33) Yue, Y. Z.; von der Ohe, R.; Jensen, S. L. *J. Chem. Phys.* **2004**, *120*, 8053. *J. Chem. Phys.* **2004**, *121*, 11508.

(34) Wang, L. M.; Velikov, V.; Angell, C. A. *J. Chem. Phys.* **2002**, *117*, 10184.

(35) Dudowicz, J.; Freed, K. F.; Douglas, J. F. *J. Phys. Chem. B* **2005**, *109*, 21350.

(36) Angell, C. A.; Moynihan, C. T.; Hemmati, M. *J. Non-Cryst. Solids* **2000**, *274*, 319.

(37) Döß, A.; Hinze, G.; Schiener, B.; Hemberger, J.; Böhmer, R. *J. Chem. Phys.* **1997**, *107*, 1740.

(38) Greaves, G. N.; Greer, A. L.; Lakes, R. S.; Rouxel, T. *Nat. Mater.* **2011**, *10*, 823.

(39) Goesten, M. G.; Stavitski, E.; Pidko, E. A.; Gucuyener, C.; Boshuizen, B.; Ehrlich, S.; Hensen, E. J. M.; Kapteijn, F.; Gascon, J. *Chem. - Eur. J.* **2013**, *19*, 7809.

(40) Allan, P. K.; Chapman, K. W.; Chupas, P. J.; Hriljac, J. A.; Renouf, C. L.; Lucas, T. C. A.; Morris, R. E. *Chem. Sci.* **2012**, *3*, 2559.

(41) Cliffe, M. J.; Wan, W.; Zou, X. D.; Chater, P. A.; Kleppe, A. K.; Tucker, M. G.; Wilhelm, H.; Funnell, N. P.; Coudert, F. X.; Goodwin, A. L. *Nat. Commun.* **2014**, *5*, 4176.

(42) Keen, D. A.; Goodwin, A. L. *Nature* **2015**, *521*, 303.

(43) Bennett, T. D.; Cheetham, A. K. *Acc. Chem. Res.* **2014**, *47*, 1555.

(44) Farrow, C. L.; Juhas, P.; Liu, J. W.; Bryndin, D.; Bozin, E. S.; Bloch, J.; Proffen, T.; Billinge, S. J. L. *J. Phys.: Condens. Matter* **2007**, *19*, 335219.

(45) Wright, A. C. *J. Non-Cryst. Solids* **1994**, *179*, 84.

(46) Baxter, E.; Bennett, T. D.; Mellot-Draznieks, C.; Gervais, C.; Blanc, F.; Cheetham, A. K. *Phys. Chem. Chem. Phys.* **2015**, *17*, 25191.

(47) Solum, M. S.; Altmann, K. L.; Strohmeier, M.; Berges, D. A.; Zhang, Y. L.; Facelli, J. C.; Pugmire, R. J.; Grant, D. M. *J. Am. Chem. Soc.* **1997**, *119*, 9804.

(48) Haines, J.; Levelut, C.; Isambert, A.; Hebert, P.; Kohara, S.; Keen, D. A.; Hammouda, T.; Andrault, D. *J. Am. Chem. Soc.* **2009**, *131*, 12333.

(49) Keen, D. A.; Goodwin, A. L.; Tucker, M. G.; Hriljac, J. A.; Bennett, T. D.; Dove, M. T.; Kleppe, A. K.; Jephcoat, A. P.; Brunelli, M. *Phys. Rev. B: Condens. Matter Mater. Phys.* **2011**, *83*, 064109.

(50) Tan, J. C.; Cheetham, A. K. *Chem. Soc. Rev.* **2011**, *40*, 1059.

(51) Atanacio, A. J.; Latella, B. A.; Barbé, C. J.; Swain, M. V. *Surf. Coat. Technol.* **2005**, *192*, 354.

(52) Mauro, J. C.; Yue, Y. Z.; Ellison, A. J.; Gupta, P. K.; Allan, D. C. *Proc. Natl. Acad. Sci. U. S. A.* **2009**, *106*, 19780.

(53) Wharmby, M. T.; Henke, S.; Bennett, T. D.; Bajpe, S. R.; Schwedler, I.; Thompson, S. P.; Gozzo, F.; Simoncic, P.; Mellot-Draznieks, C.; Tao, H.; Yue, Y. Z.; Cheetham, A. K. *Angew. Chem., Int. Ed.* **2015**, *54*, 6447.

(54) Soper, A. K. *GudrunN and GudrunX: Programs for Correcting Raw Neutron and X-Ray Diffraction Data to Differential Scattering Cross Section*; Rutherford Applied Laboratory Technical Report RAL-TR-2011-013; Science and Technology Facilities Council: Harwell, U.K., 2011.

(55) Keen, D. A. *J. Appl. Crystallogr.* **2001**, *34*, 172.

(56) Soper, A. K.; Barney, E. R. *J. Appl. Crystallogr.* **2011**, *44*, 714.

(57) Macrae, C. F.; Bruno, I. J.; Chisholm, J. A.; Edgington, P. R.; McCabe, P.; Pidcock, E.; Rodriguez-Monge, L.; Taylor, R.; van de Streek, J.; Wood, P. A. *J. Appl. Crystallogr.* **2008**, *41*, 466.

(58) Oliver, W. C.; Pharr, G. M. *J. Mater. Res.* **2004**, *19*, 3.

(59) Fung, B. M.; Khitrin, A. K.; Ermolaev, K. *J. Magn. Reson.* **2000**, *142*, 97.

(60) Morcombe, C. R.; Zilm, K. W. *J. Magn. Reson.* **2003**, *162*, 479.

(61) Bertani, P.; Raya, J.; Bechinger, B. *Solid State Nucl. Magn. Reson.* **2014**, *61−62*, 15.